

Supplement of The Cryosphere, 14, 1225–1244, 2020  
<https://doi.org/10.5194/tc-14-1225-2020-supplement>  
© Author(s) 2020. This work is distributed under  
the Creative Commons Attribution 4.0 License.



*Supplement of*

## **Multi-physics ensemble snow modelling in the western Himalaya**

**David M. W. Pritchard et al.**

*Correspondence to:* David M. W. Pritchard ([david.pritchard@newcastle.ac.uk](mailto:david.pritchard@newcastle.ac.uk))

The copyright of individual parts of the supplement might differ from the CC BY 4.0 License.

## Supplement to: Multi-physics ensemble snow modelling in the western Himalaya

### S1 Climate Input Strategies

The baseline climate inputs for this study are based primarily on downscaling and bias correction (for temperature) of the High Asia Refined Analysis (HAR, Maussion et al., 2014) dynamical downscaling product, as described in Section 3.2. Given the uncertainties in climate input fields in this data-sparse context, simulations were also performed using two alternative input derivation strategies (Section 3.2.3). These strategies are summarised in Table S1 below. The strategies are not independent, as their main purpose is to indicate whether the conclusions reached on snowpack process representations, the focus of this study, are unduly affected by the downscaling and bias correction approaches described in Section 3.2.2. Precipitation is kept consistent between strategies, as the HAR represents by far the best available source of distributed precipitation fields (Pritchard et al., 2019). The focus is thus on climate variables used in surface energy balance calculations. The implications of using these alternative input strategies are discussed in Section 5 and Section S5.

Input Strategy	Description
1	Downscaled HAR using approach described in Section 3.2.2, with simple bias correction of temperature fields. This is considered to be the best approach with available data and thus the baseline for the study.
2	Downscaled HAR using approach described in Section 3.2.2, but without any bias correction of temperature fields. The primary purpose of this strategy (2) is to check whether the temperature bias correction applied in (1) alters inter-variable relationships in a way which affects ensemble structure.
3	Downscaled HAR precipitation as per Section 3.2.2, but with other climate fields estimated primarily from observations. Specifically, temperature is lapsed based on observations (separately for daily minima and maxima, using monthly lapse rates). Daily temperatures are disaggregated to an hourly interval based on normalised climatological hourly diurnal cycle from EvK2CNR stations for each month. Relative humidity is estimated from daily minimum and maximum observations, and disaggregated to an hourly time step using a similar approach. Incoming shortwave radiation is calculated as per strategies (1) and (2). However, rather than estimating cloud transmissivity from the HAR (Section 3.2.2), a parameterisation of cloud transmissivity based on diurnal temperature range is used following calibration with local data (Pellicciotti et al., 2011). Incoming longwave radiation is estimated using the formulation from MicroMet (Liston and Elder, 2006). Wind speed is based on the HAR in the absence of observations, as per strategies (1) and (2).

**Table S1.** Summary of baseline and alternative climate input data sources and strategies.

### 15 S2 MODIS Land Surface Temperature (LST) Validation

Figure S1 compares MODIS MOD11A1 Collection 6 land surface temperature (LST) with observations from the EvK2CNR Concordia site (Figure 1b), in order to provide further validation of the remote sensing product in this region (Section 3.3). Observed LST was estimated from measured outgoing longwave radiation at Concordia for the hours closest to the MODIS overpass times. The corresponding MODIS LST values were based on the average of the 9 pixels surrounding a station location and were corrected for elevation differences using local MODIS LST lapse rates (estimated from linear regression). Figure S1 shows that the MODIS LST shows good correspondence with observations overall, as reflected by the values lying generally close to the 1:1 line. The summary statistics in Table S2 confirm that the MODIS bias is low at the annual scale (-1.6°C for night-time and 0.5°C for daytime), although it may be slightly larger for individual seasons. Nevertheless, Table S2 indicates that MOD11A1 is likely accurate enough to estimate climatological LST to within 2-3°C, depending on season.

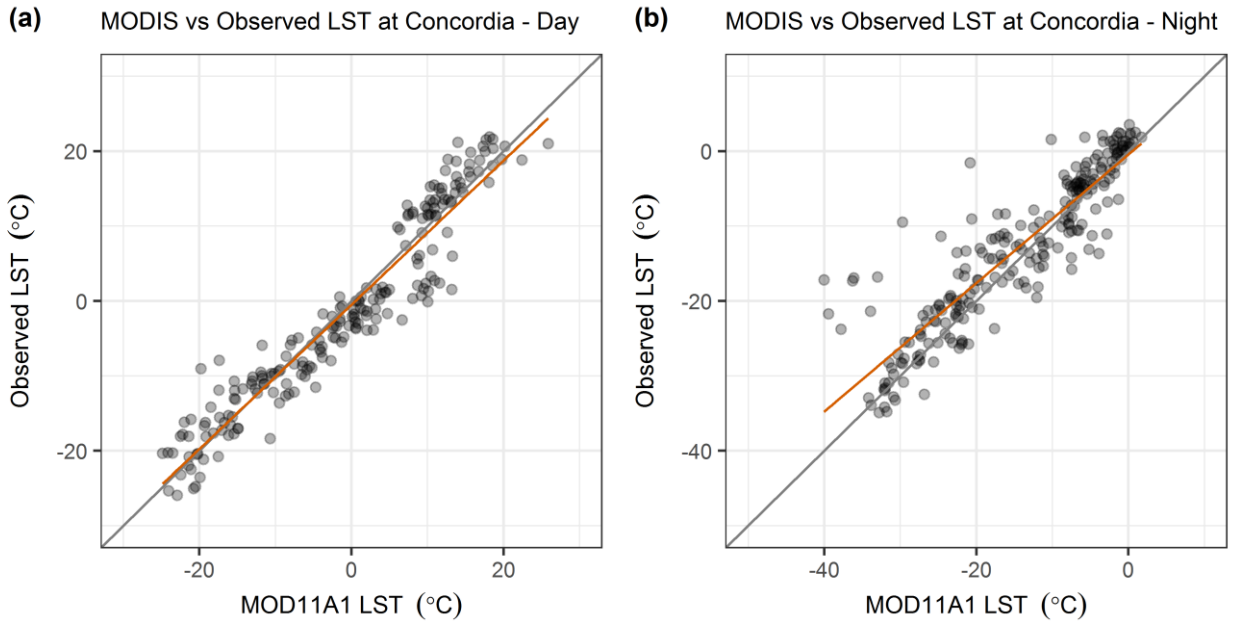


**Figure S1.** Comparison of (a) daytime and (b) night-time LST from MODIS remote sensing (MOD11A1) with observations at the Concordia site. Observed LST was derived from measured outgoing longwave radiation for the hour closest to the MODIS overpass time. The orange lines represent best fits from linear regression.

5

Season	Bias (°C)		RMSE (°C)	
	Night	Day	Night	Day
Annual	-1.6	0.5	5.0	3.7
DJF	-3.5	-1.4	3.4	7.2
MAM	-0.2	2.1	3.6	4.7
JJA	-0.7	1.4	5.0	3.7
SON	-2.8	-1.4	2.2	4.3

**Table S2.** Summary statistics for MOD11A1 performance at the EvK2CNR Concordia site.

### S3 Simulated Albedo Evaluation

This section provides an evaluation of albedo simulated by the diagnostic and prognostic albedo parameterisations using the MODIS MCD43A3 and MOD10A1 surface albedo products. These datasets have been validated in different settings (Gascoin et al., 2017; Liu et al., 2009; Wang et al., 2012), but additional challenges are posed by complex terrain (Wen et al., 2018). The evaluation thus considers the model results and datasets in both absolute and anomaly terms. The modelled series are transformed to anomalies by subtracting the ensemble mean albedo (all members), while the two MODIS series are converted to anomalies by subtracting their respective means. The evaluation focuses on catchment-scale albedo. Spatial aggregates were only calculated when 90% of pixels had satisfactory quality data, which are defined here as any processed inversion for MCD43A3 albedo.

In absolute terms, FSM mean snow albedo from March to August exceeds MODIS by 0.07 and 0.14 for MOD10A1 and MCD43A3, respectively. This may be in part due to challenges in fully characterising albedo in complex terrain with remote

sensing (Wen et al., 2018). However, in anomaly terms, Figure S2 demonstrates that the prognostic albedo parameterisation is in reasonable agreement with MODIS. Acknowledging some timing offsets and points of divergence between the MODIS products, prognostic albedo more skilfully captures the sharp albedo increases following snowfall in the melt season. Field studies have shown these events to be an important for regional melt rate variability, especially early in the season, in accordance with the latitude ( $\sim 35^{\circ}\text{N}$ ) and continentality of the area (Hewitt, 2014). The prognostic parameterisation also generally reproduces the rate of albedo decay during melting periods in Figure S2, whereas the diagnostic parameterisation induces frequent, sharp and pronounced albedo fluctuations. These fluctuations give rise to a comparatively low albedo in the early melt season. In quantitative terms, the prognostic parameterisation outperforms the diagnostic option for the anomaly series, with an overall RMSD relative to the MOD10A1 product of 0.062 (prognostic) compared with 0.071 (diagnostic). Process-level evaluation with MODIS thus corroborates the better performance of prognostic albedo for simulating catchment SCA (Section 4.1).

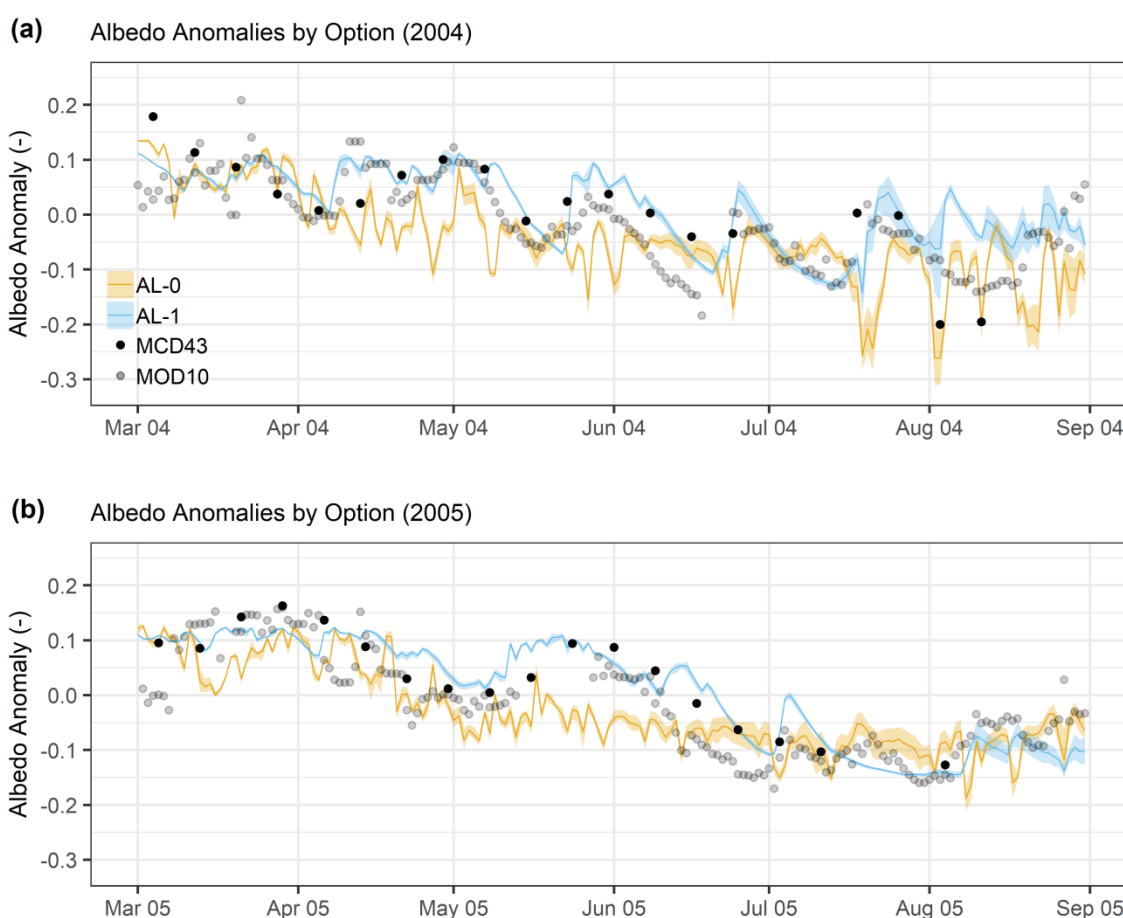


**Figure S2.** Comparison of modelled catchment-average snow albedo anomalies with MODIS remote sensing for two example melt seasons. Modelled albedo is grouped by the diagnostic (0) and prognostic (1) options in orange and blue, respectively. The mean (line) and range (shading) for the two groups are shown. MCD43A3 and MOD10A1 (8-day moving average) estimates are denoted with black and grey dots, respectively. The modelled series are converted to anomalies by subtracting the ensemble mean albedo (all members), while the MODIS series are converted by subtracting their respective means.

## S4 Model Deviations from Observations

Figure S3 shows the relationship between the root-mean-square deviation (RMSD) for cumulative snowpack runoff (simulated relative to observed total runoff) and SCA (simulated relative to MODIS), with the ensemble aggregated by albedo, liquid water and stability adjustment options. For snowpack runoff, RMSD was calculated for each year based on the cumulative runoff curves for the period between April and June. For each year, the curves were first normalised by (dividing by) their respective total runoff volumes between April and September, in order to focus on differences in timing rather than total volumes. For SCA, RMSD was calculated for the period between April and September using an NDSI threshold of zero for MODIS (see Section 3.3).

Figure S3 confirms that, for individual years as well as on average, ensemble groups exhibiting closer correspondence between snowpack runoff and observed total runoff also tend to show more consistency with MODIS SCA. This provides support for the suggestion that snowpack runoff dominates river flows in spring and early summer, with routing effects and other influences being relatively small. Figure S3 also confirms that using both prognostic albedo and the liquid water parameterisation generally leads to the best performance (Section 4.1). However, the group omitting liquid water processes but applying the stability correction also shows low mean RMSD overall, especially for SCA. As Section 4.2.3 strongly suggests the stability adjustment to be too strong in damping turbulent fluxes in stable conditions, it is possible to identify these compensatory effects as unphysical. Inter-annual variability in RMSD for all groups is high, as reflected by the wide and overlapping error bars in Figure S3. Although substantial asymmetries and trade-offs between runoff and SCA RMSDs are present, the range of RMSD tends to be smaller for groups performing better on average. However, in some years, configurations tending to perform worse on average may outperform more realistic configurations, as explored in Sections 4.4 and S5.

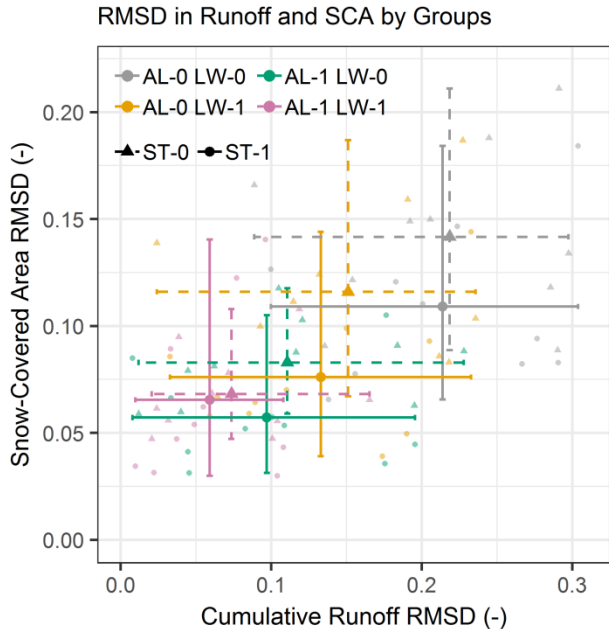


**Figure S3.** Cumulative runoff RMSD is plotted against SCA RMSD in for each of the albedo (AL) and liquid water (LW) option combinations (i.e. averaging respective ensemble members), with differentiation by stability (ST) option (shape and line type) also shown. Cumulative snowpack runoff RMSD is for the April to June period and normalised, whereas SCA RMSD is for April to September and based on an NDSI threshold of 0.

The relationships between deviations from observations for different groups of model configurations are shown in Figure S4. These relationships are portrayed as a scatterplot matrix comparing RMSD for ensemble groups using different

configurations of albedo (A), liquid water / drainage (D) and stability adjustment (S) options. The upper right of the scatterplot matrix shows runoff RMSD (noting the difference between simulated snowpack runoff and observed total runoff explained in Section 3.3), whereas the lower left shows SCA RMSD. Each point represents the RMSD for a single year, and results from all three climate input strategies are plotted (Section 3.2.3 and Section S1).

5



**Figure S4.** Scatterplot matrix comparing root-mean-square deviation (RMSD) for ensemble groups using different configurations of albedo (A), drainage (D) and stability adjustment (S) options. Scatterplots for runoff RMSD are shown in the upper right of the matrix and scatterplots for SCA RMSD are shown in the lower left. RMSD is calculated following the description in Section 4.3.1. Each point represents the RMSD for a single year, and results from all three climate input strategies are plotted (Section 3.2.3 and Section S1).

10

Figure S4 highlights the variation of performance relationships between ensemble groups. For both runoff and SCA, the most linear relationships tend to be associated with configurations using diagnostic albedo (A0). This suggests that this

choice dominates performance when selected. A relatively linear relationship (albeit with notable scatter) also occurs in the generally well-performing case where prognostic albedo and the liquid water parameterisation are both applied but the stability adjustment is varied (grey points on Figure S4). This suggests that, overall, model performance limitations are not due to varying the stability adjustment option in this case. Rather, any structural constraint on performance is common to both configurations, namely through the dominance of the albedo and snowpack hydrology parameterisations and their response to the climate conditions of a particular year.

In other cases, trade-offs resembling a Pareto front develop. Thus, for a number of the years simulated, performance in one group cannot increase without a corresponding reduction in performance of another group. For example, there are a number of years in which good performance with the liquid water option off (and the stability adjustment applied) is associated with performance reductions in more physically realistic configurations where the liquid water option is switched on. Sometimes possible Pareto-like fronts are accompanied by almost linear relationships away from the front (examples for runoff include A1D1S0 vs A1D0S0 and A1D0S1). This indicates that the relative importance of differences between ensemble groups may vary between years in some cases.

### **S5 Runoff and LST Anomaly Time Series**

Figure S5 compares simulated catchment-scale snowpack runoff and LST monthly anomalies with observed runoff and MODIS remote sensing, respectively. This demonstrates that the simulated anomalies are reasonably consistent with the reference datasets in anomaly space. The spread amongst the four major ensemble groups considered in Section 4.4 is also fairly small relative to the amplitude of inter-annual variability. Some discrepancies are of course evident, which may partly reflect the limitations of the HAR climate product in capturing the sequencing of inter-annual climate anomalies (Section 4.4). Indeed, some of the discrepancies likely fit with the SCA errors discussed in Table 3. Overall then, Figure S5 supports the finding in Section 4.4 that the FSM ensemble may be somewhat reliable in anomaly space when climate input anomalies are sufficiently represented.

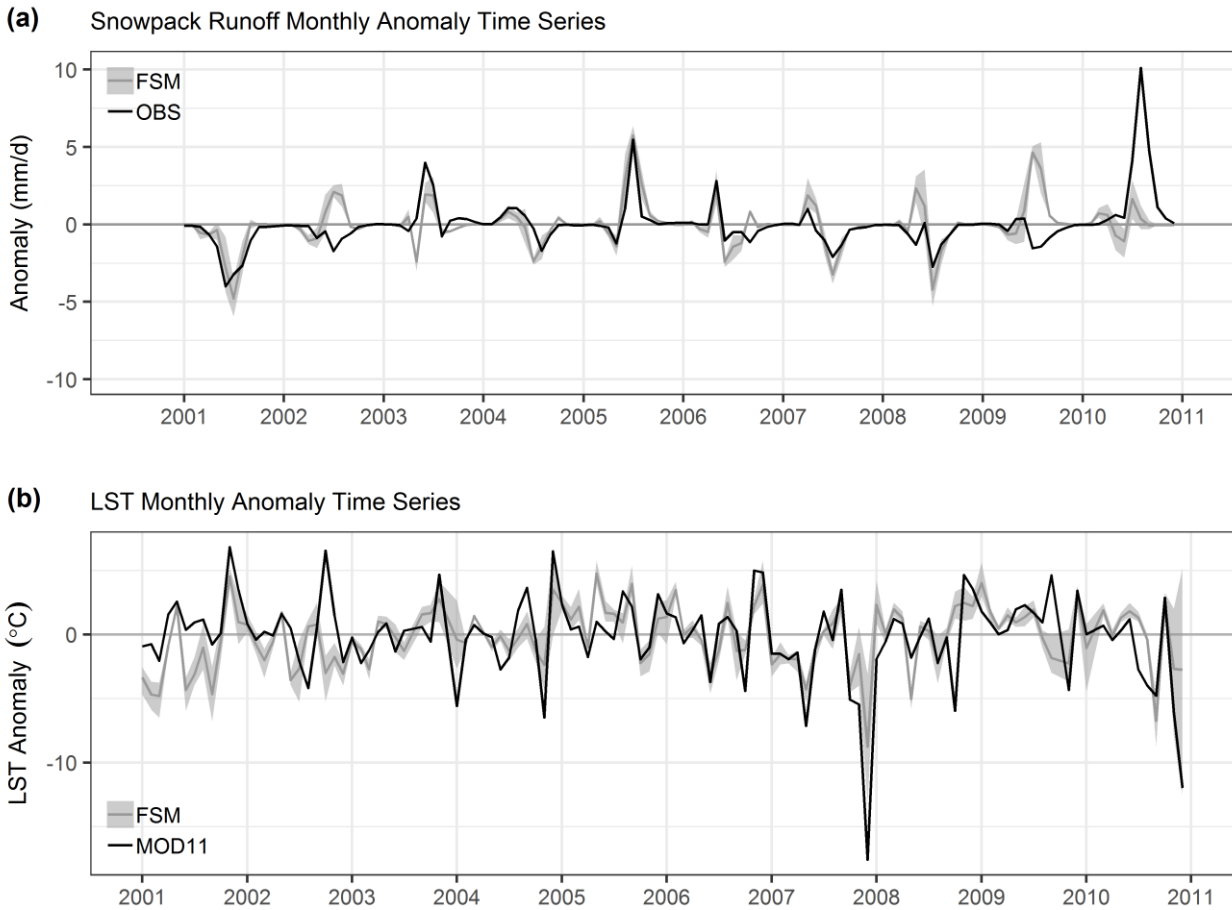
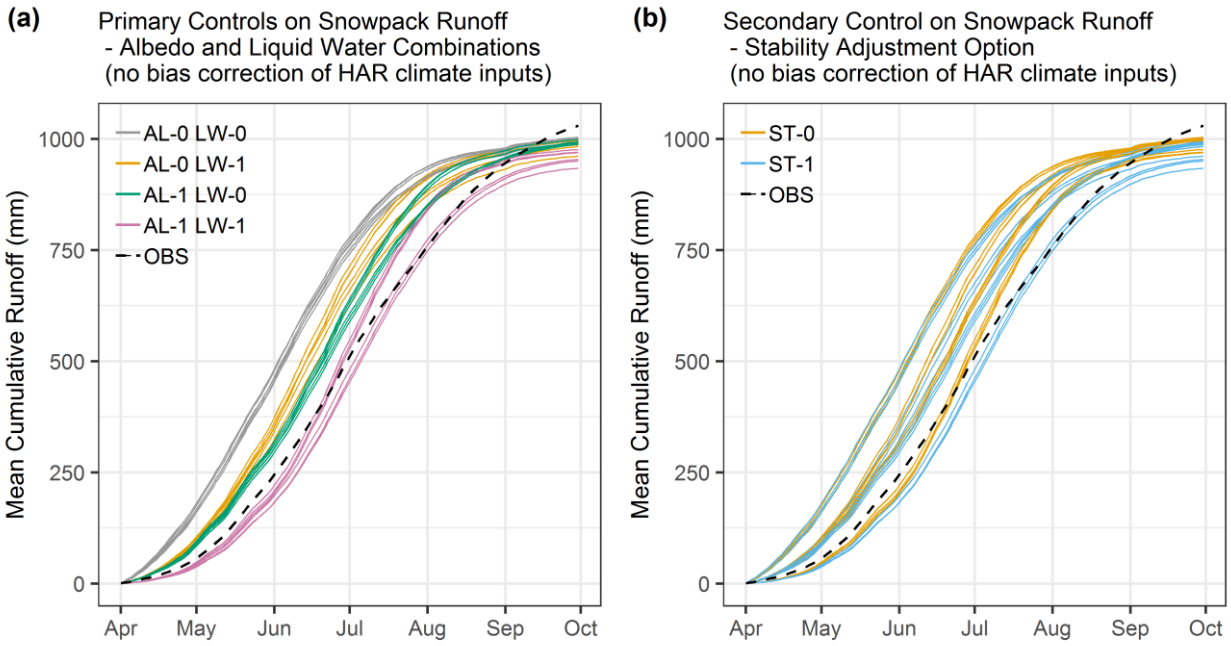


**Figure S5.** Comparison of simulated (a) runoff and (b) LST catchment-scale monthly anomalies with observations and remote sensing, respectively. The mean and range of the four primary FSM ensemble groups considered in Section 4.4 are shown by the grey lines and shading. The observations in (a) are total catchment runoff anomalies, while the simulated values are for snowpack runoff (Section 3.3).

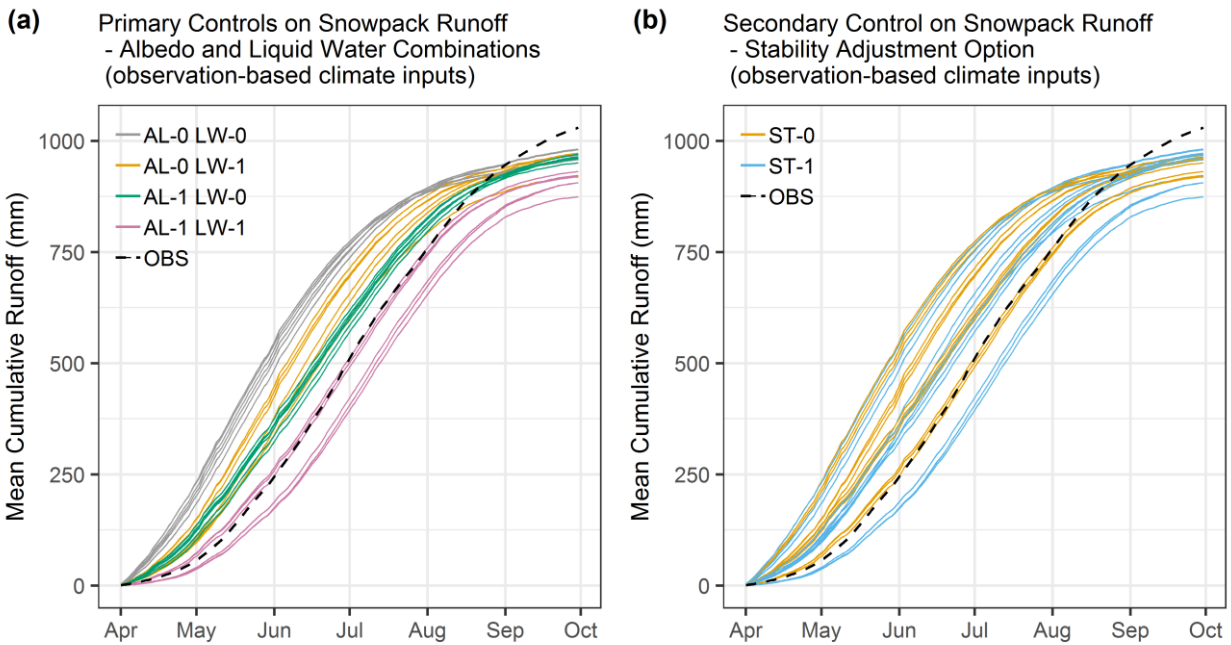
## 5 S6 Climate Input Sensitivity

Figure S6 and Figure S7 show the implications of using the two alternative climate input strategies described in Section 3.2.3 and Section S1. These strategies are essentially HAR-based inputs with no bias correction (Figure S6), and using local observations to derive climate fields as far as possible (Figure S7). Figure S6 indicates that omitting bias correction of HAR temperatures leads to a very similar ensemble structure to that presented for the baseline climate inputs in Section 4.1. There is a small shift of the cumulative snowpack runoff curves to the right in Figure S6 compared with Figure 2, which reflects the effect of the cold temperature bias in delaying runoff. However, the structure of ensemble groups matches closely in the two figures. Therefore temperature bias correction does not fundamentally alter FSM response in this case.

Figure S7 also shows notable similarity with Figure 2 in Section 4.1 in terms of overall ensemble structure. However, there is more spread within the principal groups within the ensemble in Figure S7, especially for slow-responding combinations (prognostic albedo and a representation of liquid water refreezing, retention and drainage). This leads to a wider overall ensemble spread when applying primarily observation-based inputs. Nevertheless, the rank order of the primary and secondary groups within the ensemble is the same as for the baseline climate inputs. This strengthens the notion that the findings in Section 4 are likely to be similar when using various commonly applied climate input strategies.



**Figure S6.** Comparison of mean cumulative snowpack runoff for the high-flow season for each of the 32 ensemble members with observed total runoff (OBS, black dashed line). In (a) each ensemble member is coloured according to the combination of albedo (AL) and liquid water (LW) parameterisations it uses. In (b) each ensemble member is coloured by its stability adjustment (ST) option. The results are based on input strategy (2) described in Section S1 (i.e. HAR-based but without temperature bias correction).



**Figure S7.** As Figure S6 but for input strategy (3) described in Section S1 (i.e. observation-based as far as possible).

## References

- Gascoin, S., Guðmundsson, S., Aðalgeirsdóttir, G., Pálsson, F., Schmidt, L., Berthier, E. and Björnsson, H.: Evaluation of MODIS Albedo Product over Ice Caps in Iceland and Impact of Volcanic Eruptions on Their Albedo, *Remote Sens.*, 9(399), 1–18, doi:10.3390/rs9050399, 2017.
- 5 Hewitt, K.: *Glaciers of the Karakoram Himalaya*, Springer Netherlands., 2014.
- Liston, G. E. and Elder, K.: A Meteorological Distribution System for High-Resolution Terrestrial Modeling (MicroMet), *J. Hydrometeorol.*, 7, 217–234, doi:10.1175/JHM486.1, 2006.
- Liu, J., Schaaf, C., Strahler, A., Jiao, Z., Shuai, Y., Zhang, Q., Roman, M., Augustine, J. A. and Dutton, E. G.: Validation of Moderate Resolution Imaging Spectroradiometer (MODIS) albedo retrieval algorithm: Dependence of albedo  
10 on solar zenith angle, *J. Geophys. Res.*, 114, D01106, doi:10.1029/2008JD009969, 2009.
- Maussion, F., Scherer, D., Mölg, T., Collier, E., Curio, J. and Finkelnburg, R.: Precipitation Seasonality and Variability over the Tibetan Plateau as Resolved by the High Asia Reanalysis, *J. Clim.*, 27, 1910–1927, doi:10.1175/JCLI-D-13-00282.1, 2014.
- Pellicciotti, F., Raschle, T., Huerlimann, T., Carenzo, M. and Burlando, P.: Transmission of solar radiation through  
15 clouds on melting glaciers: a comparison of parameterizations and their impact on melt modelling, *J. Glaciol.*, 57(202), 367–381, doi:https://doi.org/10.3189/002214311796406013, 2011.
- Pritchard, D. M. W., Forsythe, N., Fowler, H. J., O'Donnell, G. M. and Li, X.-F.: Evaluation of Upper Indus Near-Surface Climate Representation by WRF in the High Asia Refined Analysis, *J. Hydrometeorol.*, 20(3), 467–487, doi:10.1175/JHM-D-18-0030.1, 2019.
- 20 Wang, Z., Schaaf, C. B., Chopping, M. J., Strahler, A. H., Wang, J., Román, M. O., Rocha, A. V, Woodcock, C. E. and Shuai, Y.: Evaluation of Moderate-resolution Imaging Spectroradiometer (MODIS) snow albedo product (MCD43A) over tundra, *Remote Sens. Environ.*, 117, 264–280, doi:10.1016/j.rse.2011.10.002, 2012.
- Wen, J., Liu, Q., Xiao, Q., Liu, Q., You, D., Hao, D., Wu, S. and Lin, X.: Characterizing Land Surface Anisotropic Reflectance over Rugged Terrain: A Review of Concepts and Recent Developments, *Remote Sens.*, 10(370), 1–30,  
25 doi:10.3390/rs10030370, 2018.